Research Article

ZrMO$_X$ Particles for Enhanced Removal of Methyl Orange from Wastewater: Preparation, Characterization, and Adsorption Study

Hao Yang [ID],[1] **Yulong Sun,**[1] **Qi Zhang,**[2] **Yanfeng Pu,**[1] **Jianhong Wang** [ID],[1] **Leichang Cao,**[1] **Shuaishuai Zhou,**[1] **Qian Li,**[1] and **Congzhen Qiao**[1]

[1]*College of Chemistry and Chemical Engineering, Henan Province Engineering Research Center of Catalytic Reaction, Kaifeng, China 475004*
[2]*Puyang Lianzhong Industrial Chemical Co., Ltd., Puyang, China 457000*

Correspondence should be addressed to Jianhong Wang; jhwnj@163.com

The wide application of organic dyes in many industries has brought challenges to the effective treatment of organic wastewater. In this study, a series of ZrMO$_X$ (M: Fe, Co, Ni, Cu) particles were prepared by the coprecipitation method to adsorb methyl orange (MO) in aqueous solution. The adsorbents were characterized by X-ray diffraction (XRD), scanning electron microscopy (SEM), Fourier transform infrared spectroscopy (FT-IR), and N$_2$ adsorption-desorption. The selected adsorbent with the best adsorption performance was ZrFeO$_X$ with a molar ratio of 1 : 1 and calcination temperature of 573 K; the maximum adsorption capacity was 138.95 mg·g^{-1}. The adsorption behavior of MO onto the adsorbent was studied as a function of contact time, initial concentrations, adsorption temperature, and pH conditions. The analysis results showed that pseudo-second-order, Elovich, and Langmuir models were suitable to describe the adsorption behavior of MO on the adsorbent. In addition, regeneration experiments presented that the MO removal rate reached over 96% after repeated recycling for 5 times. The adsorbent developed in this work is not only simple to prepare and low cost but also green and energy-saving, which can make some contributions to environmental governance.

1. Introduction

Dye is a very important part of human production and life [1]. Up to now, more than 100 000 types have been discovered or invented, and over 7 000 tons of dyes are being manufactured and used yearly world widely [2]. There are about 100 tons of dye wastewater discharged into the water body every year in the process of using dyes [3]. MO belongs to the type of azo dye; it is mainly used as an acid-base indicator and biological dye. Due to the existence of the −N=N− group and the benzene ring, MO and other azo dyes are highly toxic [4, 5]. They not only cause various diseases in humans and animals but also cause harm to the environment. Therefore, it is necessary to remove MO and other dyes before the dye wastewater is discharged.

Many efforts have been made for eliminating dyes from polluted water, such as advanced oxidation technology [6], extraction [7], photocatalysis [8], and adsorption [5]. Among those, compared with the electrochemical oxidation energy consumption, extraction required more additives; photocatalysis is limited by the intensity of light. Adsorption has the advantages of mild conditions and does not need high temperature. More importantly, adsorption is a convenient, low-cost method for its extremely well-sourced adsorbent materials [9, 10].

In recent years, various adsorbent materials were discovered to the removal of dyes from wastewater. Active carbon (AC) [11–13] and modified AC [14–16] were the largest type, because they showed a high specific surface area up to 2 000 m^2·g^{-1}. MOF [17] such as UiO-66-NH$_2$ showed excellent adsorption ability to methyl orange and methylene blue, and the maximum adsorption capacities were as high as 148.4 and 549.6 mg·g^{-1}, respectively. Metal composite oxides [9, 18] and some natural products
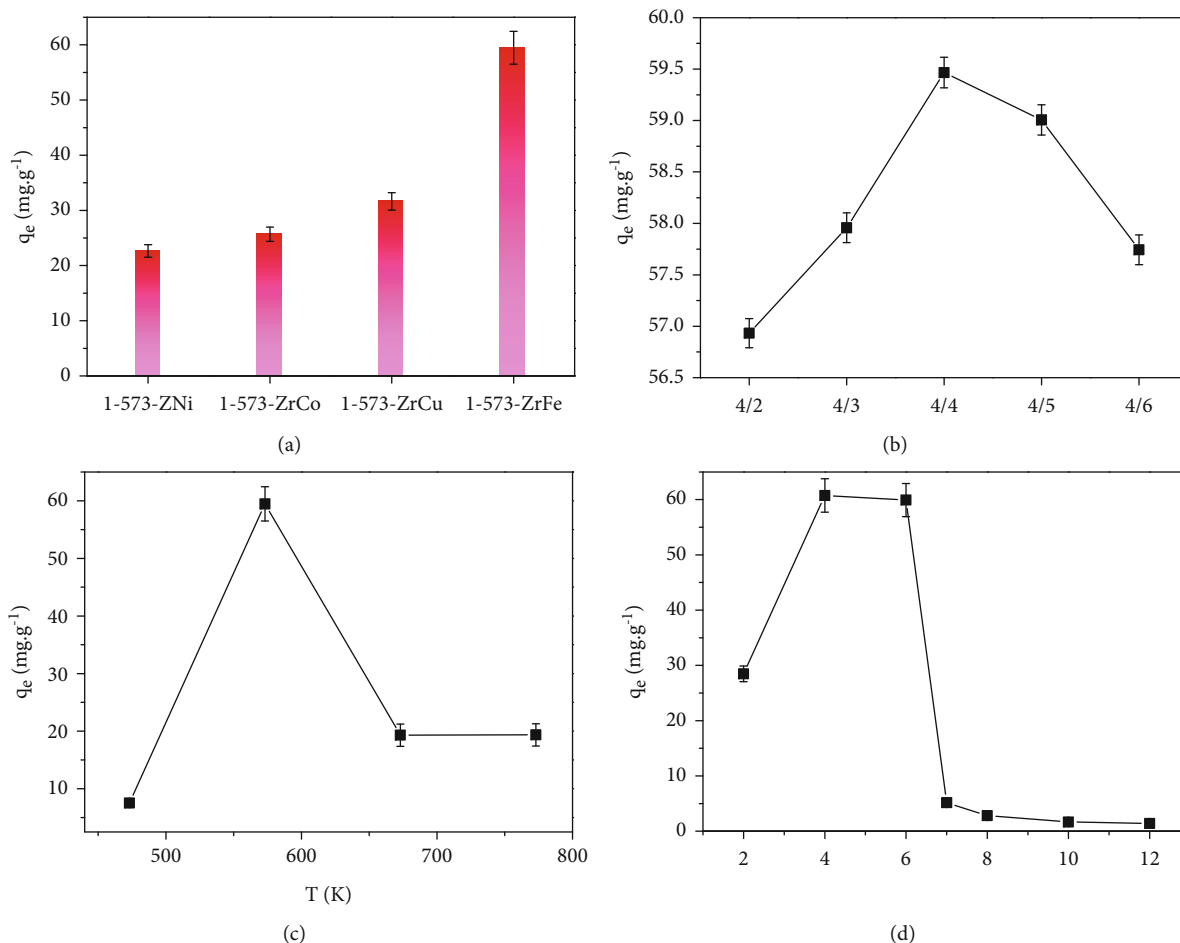
FIGURE 1: Factors affecting the adsorption performance of ZrMO$_X$: (a) different ZrMO$_X$, (b) molar ratio of Zr/Fe, (c) calcination temperature, and (d) pH of the solution (adsorption conditions of (a), (b), (c), and (d): conc.: 50 mg·L^{-1}, dose: 40 mg, T: 303 K).

[19–21] also showed excellent adsorption performance for dye absorption. However, there are many problems in adsorbents such as deficient adsorption capacity, poor regeneration performance, and loss of active components. Zirconium has good ability to accept lone pair electrons, and various coordination compounds have stable spatial structure [22, 23]. Composite oxide-based zirconium represented favorable stability against most solution systems with different acid-base properties and temperatures. The adsorbents possessed larger adsorption capacity; good stability and good reusability are optimum.

In this work, an anionic dye MO was selected as the target contaminant molecule. A series of metal composite oxides based on zirconium were prepared by the coprecipitation method as adsorbents. The materials were characterized by N$_2$ adsorption-desorption, XRD, SEM, and FT-IR. Then, the effects of contact time, adsorption temperature, pH, and initial concentration on the adsorption of adsorbents were evaluated through batch experiments. The adsorption kinetics, isotherm, and thermodynamics of the experimental data were analyzed. In addition, the regeneration performance of the adsorbent was evaluated.

2. Experimental

2.1. Materials and Methods. Ni(NO$_3$)$_2$·6H$_2$O (≥98%), Co(NO$_3$)$_2$·6H$_2$O (≥98.5%), Fe(NO$_3$)$_3$·9H$_2$O (≥98.5%), Zr(NO$_3$)$_4$·5H$_2$O (≥99%), and HCl (36%~38%) were obtained from Tianjin Kermel Chemical Reagent Co., Ltd. (Tianjin, China). Cu(NO$_3$)$_2$·3H$_2$O (≥99%) and MO (C$_{14}$H$_{14}$N$_3$SO$_3$Na, CAS No.: 547-58-0, λ_{max} = 465 nm) were purchased from Sinopharm Chemical Reagent Co., Ltd. (Shanghai, China). NH$_3$·H$_2$O (25%~28%) from Luoyang Haohua Chemical Reagent Co., Ltd. (Luoyang, China). NaOH (≥96.0%) were obtained from Tianjin Deen Chemical Reagent Co., Ltd. (Tianjin, China). Chemicals used in this work were directly used without further treatment. All water used was distilled.

2.2. Preparation of Adsorbents. Adsorbent metal composite oxides were prepared by coprecipitation [24]. 0.02 mol of M(NO$_3$)$_X$·yH$_2$O and 0.02 mol of Zr(NO$_3$)$_4$·5H$_2$O were weighed and added to 100 mL distilled water. The mixed solution was stirred for 30 min at room temperature to obtain a homogeneous solution. Precipitator (NH$_3$·H$_2$O,

TABLE 1: The surface area and pore volume parameters of four samples.

Parameters*	Adsorbents			
	Zr/Cu = 1 : 1	Zr/Co = 1 : 1	Zr/Ni = 1 : 1	Zr/Fe = 1 : 1
S_{BET} (m^2 g^{-1})	150.790	122.756	181.141	255.754
S_{mic} (m^2 g^{-1})	55.215	74.355	102.662	107.661
S_{mes} (m^2 g^{-1})	95.575	48.401	78.48	148.093
V_t (cm^3 g^{-1})	0.126	0.101	0.132	0.218
V_{mic} (cm^3 g^{-1})	0.031	0.040	0.053	0.063
V_{mes} (cm^3 g^{-1})	0.095	0.061	0.079	0.155

*S_{mic}, S_{mes}, V_{mic}, and V_{mes}: the surface area of micropore and mesopore and the volume of micropore and mesopore, respectively.
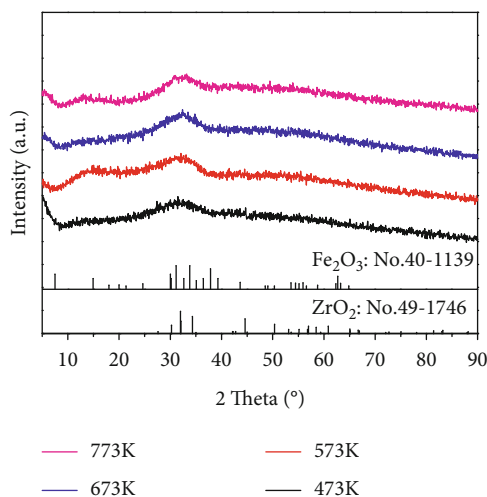
FIGURE 2: XRD patterns of four 1-ZFe calcined at different temperatures.

10% aqueous solution) was added to adjust pH of 9, then stirred 1 h, and stood for 1 h. After filtration, the residue was dried for 12 h at 353 K. Then, the obtained powders were calcined at given temperature through a 2 K·min^{-1} heating rate and holding temperature for 4 h. After selecting the ZrMO$_X$ with the highest adsorption capacity, the optimum adsorbent was selected according to the order of Zr/M molar ratio (4/2, 4/3, 4/4, 4/5, and 4/6) and calcination temperature (473 K, 573 K, 673 K, and 773 K). A series of adsorbents were obtained at various preparation conditions, which were labelled as a-b-ZM, where a and b represent the value molar ratio of Zr/M and calcination temperature, respectively.

2.3. MO Adsorption on ZrMO$_X$.
Batch experiments were carried out using a series of a 50 mL conical flask sealed with cling film. MO stock solution of 200 mg·L^{-1} was prepared through adding a certain amount of MO into distilled water. For each experiment, a certain amount of MO stock solution was diluted to required concentration. 40 mg adsorbent was added to 50 mL methyl orange solution for each adsorption test. Batch adsorption experiments were run in an air bath shaker (THZ-100, Shanghai Yiheng Instrument Co. Ltd.,

China, 160 rpm), and each batch was controlled no less than 24 h. All concentrations of MO solutions were analyzed by a dual-beam ultraviolet-visible spectrophotometer (PERSEE, TU-1900, Beijing, China). Before determination, the standard curve was plotted by the testing of standard samples, and the correlation coefficient reached 0.99. All experimental data were repeated twice in order to reduce errors. The adsorption capacity q_t (mg·g^{-1}) and equilibrium adsorption capacity q_e (mg·g^{-1}) were used to describe the performance of MO adsorption, which were calculated through Equations (1) and (2), respectively [25]:

$$q_e = \frac{(c_0 - c_e)v}{m}, \qquad (1)$$

$$q_t = \frac{(c_0 - c_t)v}{m}, \qquad (2)$$

where c_0, c_t, and c_e (mg·L^{-1}) are the MO concentrations of the moment 0, t (min), and equilibrium, respectively. v and m are the volume of MO solutions and the mass of adsorbents, respectively.

2.4. Regeneration of Adsorbents.
Regeneration study was carried out as follows. 0.5 g of used adsorbent was put into 100 mL of 0.1 M NaOH solution stirring for 1 h. The adsorbent was washed to neutrality and centrifuged out. Then, it was put into 0.001 M HCl solution containing 100 mL and stirred for 1 h, after which centrifugalization and lavation were performed. Adsorption experiment was carried out after the adsorbent was dried at 353 K for 8 h. Removal rate of MO was calculated as follows:

$$\text{Removal rate (\%)} = \frac{c_0 - c_e}{c_0} * 100. \qquad (3)$$

2.5. Characterization of Adsorbents.
Morphological features of all adsorbents in this work were examined via scanning electron microscopy (SEM) using a JSM-6700F equipment (JEOL, Japan). X-ray diffraction analysis of the adsorbents was performed with a Bruker D 8 Advance (Bruker-AXS, Germany) equipped with a copper anode (Cu Kα = 1.5406 Å). Adsorbents were scanned from 5° to 90° with a step rate of 1° s^{-1}. The results of XRD were compared with the Powder Diffraction File (PDF) database.
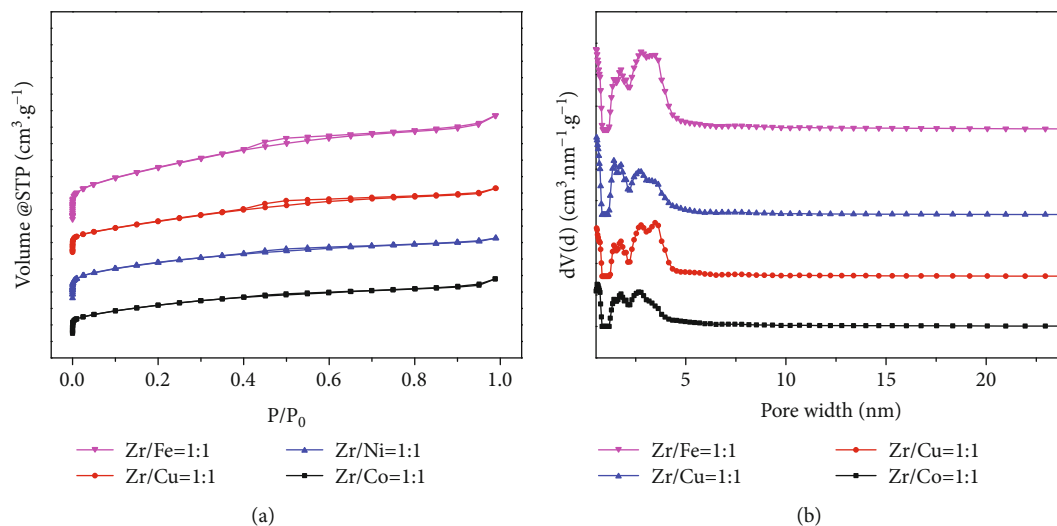
FIGURE 3: (a) N_2 adsorption-desorption isotherms and (b) the pore size distributions of four $ZrMO_X$.
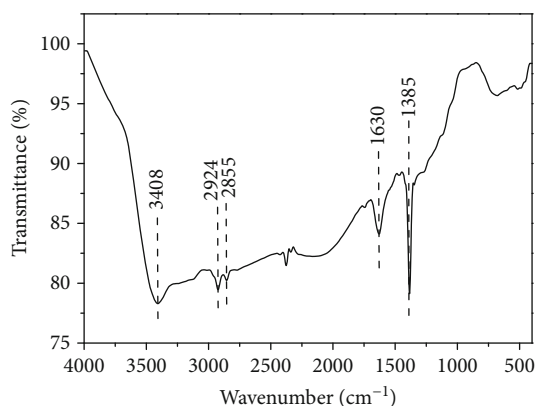
FIGURE 4: FT-IR spectra of 1-573-ZFe.

FTIR spectra of the adsorbents were acquired using a Vertex 70 spectrometer (Bruker, Germany). N_2 adsorption-desorption isotherms were investigated on Autosorb-iQ-MP-C (Quantachrome, America). All adsorbents were outgassed at 573 K for 4 h. The specific surface area (S_{BET}) and total pore volume (V_t) were calculated by the Brunauer-Emmett-Teller (BET) method, and the pore size distribution was calculated by the DFT theory.

3. Results and Discussion

3.1. Effect of the Type of $ZrMO_X$. A batch of Zr/Cu, Zr/Co, Zr/Ni, and Zr/Fe oxides with the molar ratio of 1 : 1 was prepared for equilibrium adsorption experiment. The results are shown in Figure 1(a); the equilibrium adsorption capacity of the 1-573-ZFe was the largest. Surface area and pore volume are an important indicator that affects the adsorption capacity [26]. From Table 1, it can be seen that 1-573-ZFe has abundant surface area and pore volume in the four $ZrMO_X$, which attributed to obtaining the highest equilibrium adsorption capacity among the four $ZrMO_X$.

3.2. Investigation on the Optimal Zr/Fe Molar Ratio. A series of $ZrFeO_X$ particles with different molar ratios were prepared as adsorbents to investigate the removal of MO. From Figure 1(b), it was obvious that the largest adsorption capacity was obtained at 1 : 1 of the Zr/Fe molar ratio. This situation may be caused by the synergistic effect between Zr and Fe [27]. When the Zr/Fe molar ratio was greater than 1, the synergistic effect gradually increases with the increase of Fe content, and the adsorption sites gradually increase, resulting in an increase in the equilibrium adsorption capacity. However, when the molar ratio was less than 1, iron oxides may coat the adsorption sites [28], resulting in a decrease in adsorption sites and further a reduction in the equilibrium adsorption capacity.

3.3. Effect of Calcination Temperature. The calcination temperature has a significant effect on the formation [29] and absorption efficiency of adsorbents. The adsorption properties of 1-ZFe prepared after calcination at 473 K, 573 K, 673 K, and 773 K for MO were investigated, respectively; the result is shown in Figure 1(c). It can be seen from Figure 1(c) that when calcination temperature was between 473 K and 573 K, q_e gradually increased as the temperature rose. q_e was related to the crystallinity of 1-ZFe. As calcination temperature increased, the crystallinity of 1-ZFe gradually increased. The results of XRD characterization data can well prove this point of view. Then, with the increase of temperature, q_e gradually drops to 20 mg·g^{-1}, and then, there was no significant change with the increase of temperature. When the temperature rose to 673 K, the decrease in q_e may be due to the intense agglomeration of the metal oxides at high temperature, resulting in a sharp decrease in the number of adsorption sites.

3.4. Effect of MO Solution pH. As shown in Figure 1(d), the effect of solution pH (2~12) on adsorption performance of 1-573-ZFe was tested. It can be seen that adsorption of MO on the surface of 1-573-ZFe can proceed normally under acidic conditions. However, when pH reached 7, q_e

(a)

(b)
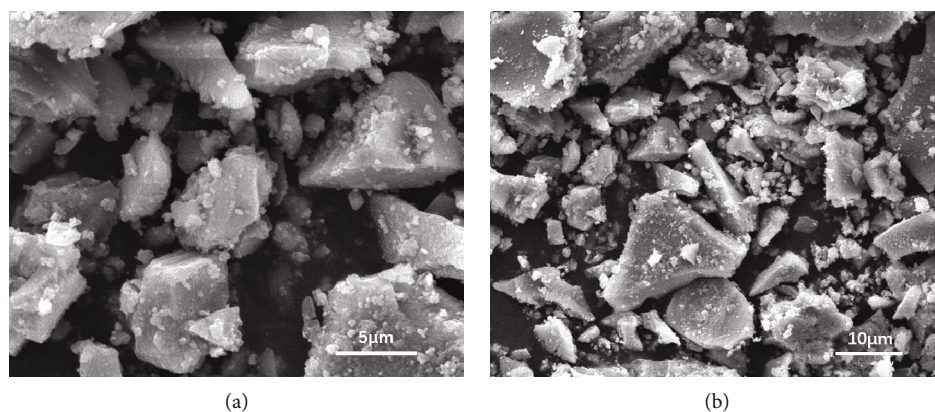
FIGURE 5: (a, b) The SEM images of 1-573-ZFe.

50 mg.L^{-1}
200 mg.L^{-1}
PFO

(a)

50 mg.L^{-1}
200 mg.L^{-1}
PSO

(b)

50 mg.L^{-1}
200 mg.L^{-1}
ELO

(c)

50 mg.L^{-1}
200 mg.L^{-1}
W-M

(d)
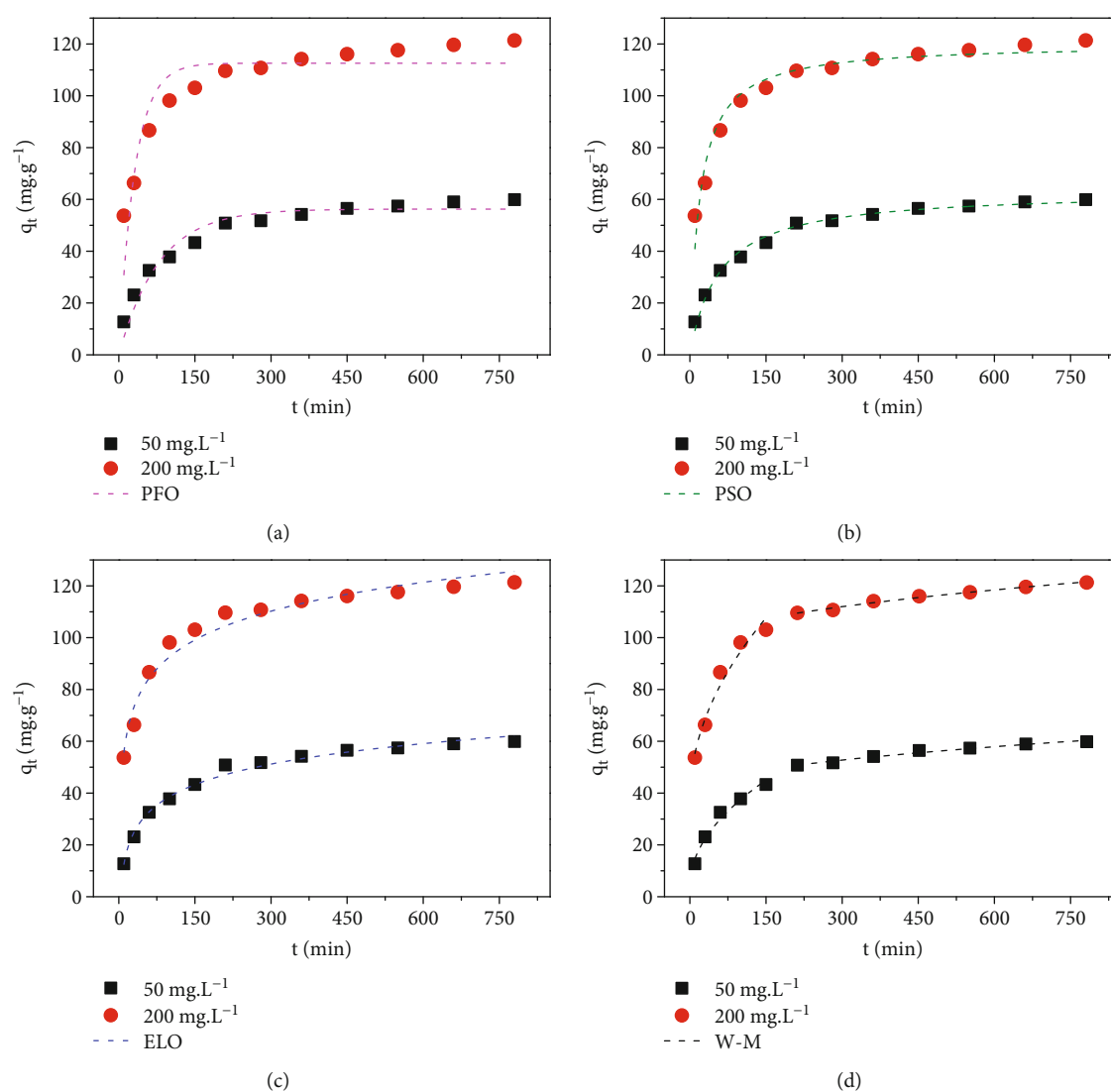
FIGURE 6: Fitted of experimental data with (a) PFO, (b) PSO, (c) ELO, and (d) W-M kinetic models.

dropped sharply to 5.14 mg·g^{-1}, and then, q_e decreased as the pH increased. When pH > 7, the sudden decrease of q_e may be due to the competitive adsorption between OH$^-$ and C$_{14}$H$_{14}$N$_3$SO$_3^-$ on the active sites of 1-573-ZFe. The OH$^-$ in

solution was easier to combine with the adsorption active sites on the surface of 1-573-ZFe. The OH$^-$ adsorbed on the active sites and the C$_{14}$H$_{14}$N$_3$SO$_3^-$ in the solution repel each other due to electrostatic interaction, so q_e decreased

TABLE 2: The fitted values of parameters in PFO, PSO, and ELO and W-M kinetic models.

Model	Parameters	50 mg·L^{-1}	200 mg·L^{-1}
PFO	k_1 (min^{-1})	0.0126	0.0318
	q_e (mg·g^{-1})	56.48	112.58
	R^2	0.9387	0.7974
PSO	k_2 (g·mg^{-1}·min^{-1})	0.0003	0.0004
	q_e (mg·g^{-1})	63.61	120.07
	R^2	0.9855	0.9428
ELO	a (mg·g^{-1} min^{-1})	0.0253	0.1989
	b (mg·g^{-1})	11.49	16.06
	R^2	0.9883	0.9650
W-M	k_{W-M-1} (mg·g^{-1}·min$^{0.5}$)	3.3439	5.7572
	I_1	4.0536	37.10
	R^2	0.9682	0.9510
	k_{W-M-2} (mg·g^{-1}·min$^{0.5}$)	0.7163	0.8998
	I_2	40.46	96.51
	R^2	0.9744	0.9859

when pH > 7. When pH met between 4 and 6, protonation of the active groups appeared on the surface of 1-573-ZFe, which increased the electron attraction with the $C_{14}H_{14}N_3SO_3^-$. So it was conducive to adsorption of MO on the 1-573-ZFe at pH of 4~6. However, q_e decreased when pH was less than 4 because of the unstable structure [30] of adsorbent under acidic conditions, which led to destruction or reduction of adsorption sites. Therefore, all adsorption experiments were carried out at the pH of 4~6 subsequently.

3.5. Characterization of ZrMO$_X$. Figure 2 shows the XRD spectrum of four 1-ZFe calcined at 473 K, 573 K, 673 K, and 773 K. It was shown that the adsorbents were amorphous. By comparing with the standard PDF card of the oxide of zirconium and iron, the peak appearing at about 32° may be contributed by Fe_2O_3 and ZrO_2 (JCPDS card No. 40-1139 and 49-1746, respectively). When the calcination temperature reached 773 K, it can be seen that there were two peaks near 32°, which may be caused by the increase of crystallinity which reflected in the (1 1 3) and (1 1 6) planes of Fe_2O_3 and the (1 2 0) and (1 1 1) planes of ZrO_2. There was no information about the broad peak near 15° related to the oxides of zirconium and iron, which was consistent with the results reported by Dou et al. [31].

N$_2$ adsorption-desorption isotherms are shown in Figure 3(a), and the adsorption of N$_2$ on ZrMO$_X$ was type IV isotherm according to IUPAC [32]. There was a hysteresis loop at relative pressure (P/P$_0$) of 0.4~0.7, which indicated the presence of mesoporous structure. It can be seen the pore size distributions of ZrMO$_X$ were centered around 3 nm from Figure 3(b). It is clear from Table 1 that the BET-specific surface area and pore volume of Zr/Fe composite oxide were the largest among the four adsorbents. The

rich specific surface area and pore volume provide sufficient locations for the adsorption of MO on ZrFeO$_X$.

Figure 4 shows the FT-IR spectrum of 1-573-ZFe. The absorption peaks at 3408 cm^{-1} and 1630 cm^{-1} were bending vibration and O-H tensile vibration of water molecules adsorbed by 1-573-ZFe, respectively [33]. The signals at 1385 cm^{-1} were attributed to the bending vibration of the Zr-OH groups [34]. The wide peak near 500 cm^{-1} was caused by the vibration of Zr-O and Fe-O bonds.

As shown in Figure 5, the morphology for 1-573-ZFe was observed by SEM. It can be seen from the figure that the size distribution of the material was wide and amorphous, and there have many particles smaller than 2 microns on the solid surface of the adsorbent. There was no obvious pore structure observed on the surface of the adsorbent. Combined with the characterization results of N$_2$ adsorption-desorption, it can be well proved that there was no macroporous structure in the adsorbent.

3.6. Adsorption Kinetics. The kinetic data was obtained under the conditions of 303 K and initial concentrations of 50 mg·L^{-1} and 200 mg·L^{-1} MO solutions. Several classical kinetic models were used in this work, such as pseudo-first-order (PFO), pseudo-second-order (PSO), and Elovich (ELO) models presented in the following (Equations (4)–(6)) [35]:

$$\ln (q_e - q_t) = \ln q_e - k_1 t, \quad (4)$$

$$\frac{t}{q_t} = \frac{1}{k_2 * q_e^2} + \frac{t}{q_e}, \quad (5)$$

$$q_t = \frac{1}{a} \ln (ab) + \frac{1}{a} \ln (t), \quad (6)$$

where q_e and c_e are as defined above; k_1 (min^{-1}) and k_2 (g·mg^{-1}·min^{-1}) are the rate constants of pseudo-first-order and pseudo-second-order, respectively; a (mg·g^{-1}) is the parameter about the surface coverage and adsorption free energy in the chemisorption; b (mg·g^{-1}·min^{-1}) is the initial sorption rate.

Fitting parameters of PFO, PSO, and ELO kinetic models for MO adsorption are shown in Figure 6 and Table 2. It can be seen from Figure 6 that no matter the initial concentration was 50 mg·L^{-1} or 200 mg·L^{-1}, there was a fast adsorption rate in the initial stage of adsorption, and the adsorption was almost completed within 300 minutes. Combined with the chart, the kinetic models of PSO and ELO are more consistent with experimental data than PSO. It can be explained that the rate-limiting step was chemical adsorption [36] on the heterogeneous interface of 1-573-ZFe [37].

In general, the Weber and Morris model (W-M) was often applied to fit the kinetic data in order to deduce the rate-limiting step [32], expressed as Equation (7) [38]:

$$q_t = k_{W-M-n} t^{0.5} + I_n, \quad (7)$$

where k_{W-M-n} (mg·g^{-1} min$^{-0.5}$, n is the number stage) is the rate constant of intraparticle diffusion kinetic model; I_n (mg·g^{-1}) is a proportional constant to the boundary layer thickness.
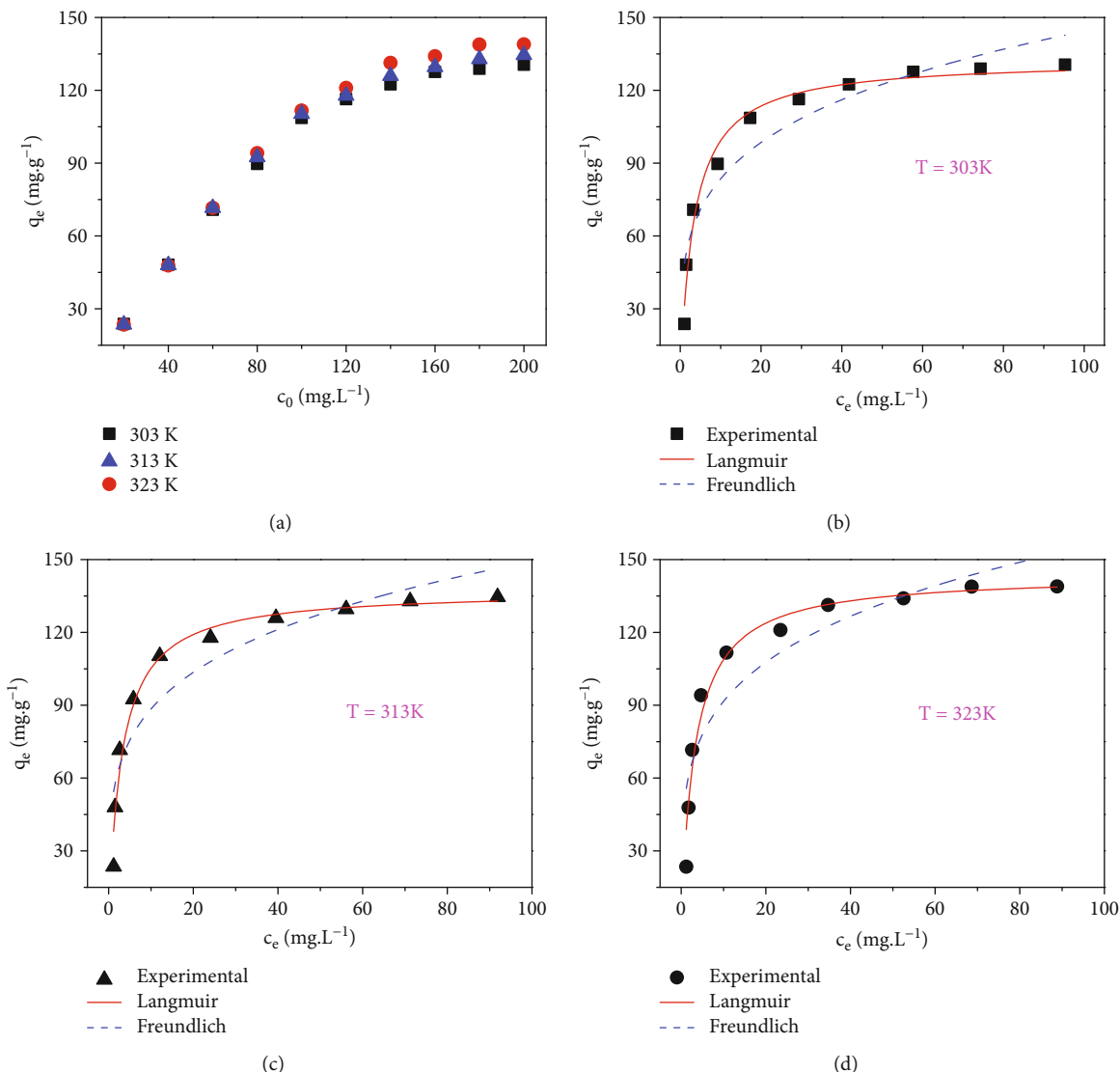
FIGURE 7: Experimental adsorption isotherms of MO adsorption on 1-573-ZFe at 303-323 K (a) and their correlation with Langmuir and Freundlich adsorption models (b, c, and d).

It can be seen from the multisegment fitting diagram in Figure 6(d) that the adsorption process of MO on 1-573-ZFe has undergone two stages of film diffusion and pore diffusion; Qian et al. [39] adsorption of haloforms on granular activated carbon and Liu et al. [30] adsorption of MO on $FeOCl-MoS_2$ both observed similar phenomena. Surface adsorption occurs first in the first stage, and the MO in the solution rapidly diffuses and adsorbs to the surface of 1-573-ZFe, resulting in a larger value of k_{W-M-2}. The second stage was the intraparticle diffusion. MO diffuses into the interior of 1-573-ZFe and was adsorbed on the internal adsorption active sites. The intraparticle diffusion stage was a gradual process, which can be obtained from k_{W-M-2} in Table 2. Since the fitted line did not cross the origin, it indicated that the intraparticle diffusion was not the rate-limiting step of adsorption [35].

3.7. Adsorption Isotherms. Adsorption isotherm is an important factor of adsorption performance. Adsorption isotherm demonstrates the relationship curve between q_e and c_e at a certain temperature. Langmuir and Freundlich isotherm models were used to fit the equilibrium data of the temperature at 303 K, 313 K, and 323 K. The equations can be expressed as Equations (8) and (9) [40]:

$$q_e = \frac{K_L * q_m * c_e}{1 + K_L * c_e}, \tag{8}$$

$$q_e = K_F * c_e^{1/n}, \tag{9}$$

where K_L (L·mg⁻¹) and K_F (L·mg⁻¹) are the constants of Langmuir and Freundlich adsorption isotherm models, respectively; q_m (mg·g⁻¹) relates to the theoretical maximum

Table 3: The fitted values of parameters in Langmuir and Freundlich models for MO adsorption.

Models	Parameters	303 K	313 K	323 K
Langmuir	K_L (L·mg^{-1})	0.2981	0.3277	0.3116
	q_m (mg·g^{-1})	132.55	137.29	143.68
	R^2	0.9788	0.9737	0.9693
Freundlich	K_F (L·mg^{-1})	48.37	52.48	53.52
	n	0.2375	0.2269	0.2335
	R^2	0.8926	0.8439	0.8326

Table 4: Thermodynamic parameters for adsorption of MO on 1-573-ZFe.

T (K)	ln K	ΔG (J·mol^{-1})	ΔS (J·mol^{-1}·K^{-1})	ΔH (J·mol^{-1})	R^2
303	1.8399	-4640.30			
313	1.9307	-5012.51	37.22	6637.65	0.9978
323	2.0029	-5384.72			
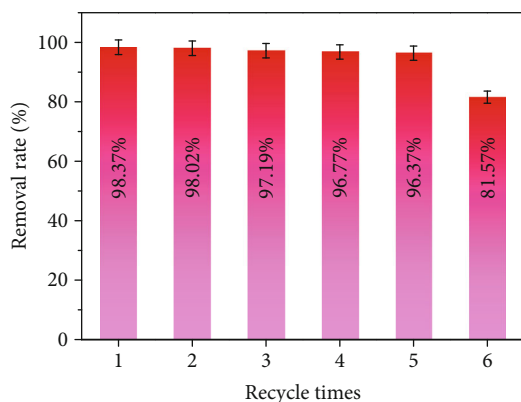
Figure 8: Regeneration efficiency from batch experiments for 6 consecutive cycles of regeneration of 1-573-ZFe.

adsorption capacity; $1/n$ is the adsorption intensity factor; n depends on the property, intensity in the adsorption process, and distribution of active sites.

As shown in Figure 7(a), it can be seen that q_e increased with the increasing of temperature, and it can be inferred that the adsorption process was endothermic [41]. Not only that, but it can also be seen that when the initial concentration is 20~60 mg·L^{-1}, q_e was not significantly affected by temperature and remains almost unchanged. It can be considered that this material has a wide temperature operating range at low MO concentrations. From Figures 7(b)–7(d) and Table 3, it can be seen that Langmuir adsorption isotherm was better fitted to the adsorption process. This showed that the adsorption behavior of MO on 1-573-ZFe was a monolayer adsorption [42], and it was calculated that the maximum adsorption capacity of MO on 1-573-ZFe surface was 143.68 mg·g^{-1}.

3.8. Adsorption Thermodynamics. In order to obtain the change of energy in the adsorption process, thermodynamic

experiments were carried out at the temperature of 303 K, 313 K, and 323 K, respectively. The changes of thermodynamic parameters of Gibbs free energy (ΔG), enthalpy (ΔH), and entropy (ΔS) were calculated by using the following:

$$
\begin{aligned}
\Delta G &= \Delta H - T\Delta S, \\
\ln K &= \frac{\Delta S}{R} - \frac{\Delta H}{RT}, \\
K &= \frac{q_e}{c_e},
\end{aligned}
\tag{10}
$$

where K is the thermodynamic equilibrium constant; T (K) is the thermodynamic temperature; R (8.314 J·mol^{-1}·K^{-1}) is the molar gas constant. ΔH (J·mol^{-1}) and ΔS (J·mol^{-1}) were calculated based on the linear relationship between ln K and $1/T$. The thermodynamic parameters are listed in Table 4.

It can be seen from Table 4 that ΔG was between -10 and 0 kJ·mol^{-1}, indicating that the adsorption process under the experimental conditions was a spontaneous physical adsorption process [43, 44]. Moreover, ΔG decreased with the increasing of temperature, which further verified that the increasing of temperature improved adsorption. The adsorption enthalpy of MO on 1-573-ZFe was positive, indicating that the adsorption process was endothermic. This may be because the interaction of MO molecules with the adsorption sites on the surface of 1-573-ZFe was weaker than that of water molecules [44]. The adsorption of MO on 1-573-ZFe required the desorption of water molecules firstly, so the adsorption took place based on absorption of heat. The change of adsorption entropy was positive, indicating that the spontaneous adsorption of MO on 1-573-ZFe was an entropy-controlled process [45], and the randomness of the solid-liquid interface increases [37].

3.9. Regeneration Performance. The regeneration of the adsorbent is an important indicator to judge whether it can be used as an industrial adsorbent. After the regeneration experiment was finished, 1-573-ZFe was directly used for readsorption of MO. The result is shown in Figure 8. It can be seen from the figure that although the removal rate of MO gradually decreases with the increase of the number of cycles, the results of the fifth cycle regeneration test show that the removal rate of MO can reach 96.37%. Even after the sixth time, the MO removal rate can still reach more than 80%. These results demonstrated that 1-573-ZFe not only has good regeneration stability but also has good application potential in environmental remediation.

In Table 5, the adsorption capacities of MO were compared between this work and other reported adsorbents. The adsorbents were often modified through some processes to increase their adsorption capacity for MO. By comparison, it can be seen that the 1-573-ZFe adsorbent reported in this work has good adsorption capacity. Moreover, the preparation method is simple, the economic cost is low, and the energy consumption is low. It is an adsorbent with good commercial application value.

TABLE 5: Comparison of MO adsorption capacity for various adsorbents.

Adsorbent	q_e (mg·g^{-1})	Conditions	Reference
Bottom ash	8.31	303 K	[46]
N–TiO$_2$	8.9	303 K	[43]
Polyaniline/emulsion microsphere	147.93	298 K; dose: 2 g·L^{-1}; conc: 0.1 mM	[47]
Modified ultrafine coal powder	18.52	303 K	[48]
Magnetic chitosan	425	318 K	[49]
Co$_3$O$_4$ nanoparticles	3.23	303 K; dose: 0.1 g·L^{-1}; pH 6	[50]
1-573-ZFe	138.95	323 K; conc: 40 mg·L^{-1}; dose: 0.8 g·L^{-1}	This work

4. Conclusion

In summary, among the four ZrMO$_X$ adsorbents prepared by the coprecipitation method, through step-by-step screening, 1-573-ZFe showed best adsorption performance when the pH was between 4 and 6; this may be due to their high BET surface area (255.754 m^2·g^{-1}) and pore volume (0.218 cm^3·g^{-1}). It can be seen from the XRD and SEM characterization results that 1-ZFe is an amorphous composite metal oxide with irregular structure. The experimental data of kinetics and PSO and ELO can describe the dynamic adsorption process of MO on 1-573-ZFe, indicating that the adsorption of MO on 1-573-ZFe was a chemical adsorption control process that occurs on a heterogeneous surface. When the MO concentration is 0~60 mg·L^{-1}, the temperature change has almost no effect on the equilibrium adsorption capacity, and the removal rate of MO can reach more than 94%. The isotherm model indicated that MO has a monolayer adsorption on the 1-573-ZFe surface. The thermodynamic parameter ΔG was between -10 and 0 kJ·mol^{-1}, indicating that the process was a spontaneous physical adsorption. Both ΔH and ΔS were positive, explaining that the adsorption process was endothermic and controlled by entropy. The removal rate of MO can be over 96% after 5 times of regeneration, which explained 1-573-ZFe has superior regeneration performance. Therefore, these results indicated that 1-573-ZFe present excellent prospects on the removal of organic pollutants from wastewater.

Data Availability

The data used to support the findings of this study are included within the article.

Conflicts of Interest

The authors declare that they have no conflicts of interest.

Authors' Contributions

Ms. Yulong Sun contributed equally to this work and should be considered co-first author.

Acknowledgments

References

[1] N. Chaukura, E. C. Murimba, and W. Gwenzi, "Synthesis, characterisation and methyl orange adsorption capacity of ferric oxide-biochar nano-composites derived from pulp and paper sludge," *Applied Water Science*, vol. 7, pp. 2175–2186, 2017.

[2] H. Zhu, R. Jiang, J. Li, Y. Fu, S. Jiang, and J. Yao, "Magnetically recyclable Fe$_3$O$_4$/Bi$_2$S$_3$ microspheres for effective removal of Congo red dye by simultaneous adsorption and photocatalytic regeneration," *Separation and Purification Technology*, vol. 179, pp. 184–193, 2017.

[3] M. T. Yagub, T. K. Sen, S. Afroze, and H. M. Ang, "Dye and its removal from aqueous solution by adsorption: a review," *Advances in Colloid and Interface Science*, vol. 209, pp. 172–184, 2014.

[4] A. Meng, J. Xing, Z. Li, and Q. Li, "Cr-doped ZnO nanoparticles: synthesis, characterization, adsorption property, and recyclability," *ACS Applied Materials & Interfaces*, vol. 7, pp. 27449–27457, 2015.

[5] S. Pandey, "A comprehensive review on recent developments in bentonite-based materials used as adsorbents for wastewater treatment," *Journal of Molecular Liquids*, vol. 241, pp. 1091–1113, 2017.

[6] G. Wang, Y. Liu, J. Ye, Z. Lin, and X. Yang, "Electrochemical oxidation of methyl orange by a Magnéli phase Ti$_4$O$_7$ anode," *Chemosphere*, vol. 241, p. 125084, 2020.

[7] M. del Rio, J. C. Grimalt Escarabajal, G. Turnes Palomino, and C. Palomino Cabello, "Zinc/iron mixed-metal MOF-74 derived magnetic carbon nanorods for the enhanced removal of organic pollutants from water," *Chemical Engineering Journal*, vol. 428, p. 131147, 2022.

[8] H. Tang, Z. Tang, J. Bright et al., "Visible-light localized surface plasmon resonance of WO$_{3-x}$ nanosheets and its photocatalysis driven by plasmonic hot carriers," *ACS Sustainable Chemistry & Engineering*, vol. 9, pp. 1500–1506, 2021.

[9] M. Arshadi, F. Mousavinia, M. J. Amiri, and A. R. Faraji, "Adsorption of methyl orange and salicylic acid on a nano-transition metal composite: kinetics, thermodynamic and electrochemical studies," *Journal of Colloid and Interface Science*, vol. 483, pp. 118–131, 2016.

[10] S. Pandey, E. Fosso-Kankeu, M. J. Spiro et al., "Equilibrium, kinetic, and thermodynamic studies of lead ion adsorption from mine wastewater onto MoS_2-clinoptilolite composite," *Materials Today Chemistry*, vol. 18, p. 100376, 2020.

[11] S. Rattanapan, J. Srikram, and P. Kongsune, "Adsorption of methyl orange on coffee grounds activated carbon," in *2017 International Conference on Alternative Energy in Developing Countries and Emerging Economies*, J. Waewsak, K. Sangkharak, S. Othong, and Y. Gagnon, Eds., vol. 138, pp. 949–954, Energy Procedia, 2017.

[12] H. Wang, J. Li, W. Liu et al., "Preparation of novel carbon spheres based on molecular design and adsorption/degradation of methyl orange," *Journal of Dispersion Science and Technology*, vol. 41, no. 7, pp. 980–991, 2020.

[13] K. Xia, G. Wang, H. Zhang et al., "Synthesis of bimodal mesoporous carbon nanospheres for methyl orange adsorption," *Journal of Porous Materials*, vol. 24, pp. 1605–1612, 2017.

[14] T. Jiang, Y.-d. Liang, Y.-j. He, and Q. Wang, "Activated carbon/$NiFe_2O_4$ magnetic composite: a magnetic adsorbent for the adsorption of methyl orange," *Journal of Environmental Chemical Engineering*, vol. 3, pp. 1740–1751, 2015.

[15] Y.-z. Ma, D.-f. Zheng, Z.-y. Mo, R.-j. Dong, and X.-q. Qiu, "Magnetic lignin-based carbon nanoparticles and the adsorption for removal of methyl orange," *Colloids and Surfaces a-Physicochemical and Engineering Aspects*, vol. 559, pp. 226–234, 2018.

[16] E. Pargoletti, V. Pifferi, L. Falciola et al., "A detailed investigation of MnO_2 nanorods to be grown onto activated carbon. High efficiency towards aqueous methyl orange adsorption/degradation," *Applied Surface Science*, vol. 472, pp. 118–126, 2019.

[17] S.-W. Lv, J.-M. Liu, H. Ma et al., "Simultaneous adsorption of methyl orange and methylene blue from aqueous solution using amino functionalized Zr-based MOFs," *Microporous and Mesoporous Materials*, vol. 282, pp. 179–187, 2019.

[18] N. Duan, Q. Li, J. Liu, and H. Xiao, "Enhanced adsorption performance of $CuO-Al_2O_3$ composite derived from cotton template," *Canadian Journal of Chemical Engineering*, vol. 93, pp. 2015–2023, 2015.

[19] A. N. M. A. Haque, R. Remadevi, X. Wang, and M. Naebe, "Adsorption of anionic acid blue 25 on chitosan-modified cotton gin trash film," *Cellulose*, vol. 27, pp. 9437–9456, 2020.

[20] A. Kassale, K. Barouni, M. Bazzaoui, J. I. Martins, and A. Albourine, "Methylene blue adsorption by cotton grafted with succinic anhydride," *Protection of Metals and Physical Chemistry of Surfaces*, vol. 51, pp. 382–389, 2015.

[21] Y. Liu, L. Xia, H. Guo et al., "Kinetics and Thermodynamics Studies of Cationic Dye Adsorption onto Carboxymethyl Cotton Fabric," *Journal of Natural Fibers*, vol. 19, pp. 173–184, 2022.

[22] W. Deng and Y. Li, "High-temperature electrical properties of polycrystalline MgO-doped ZrO_2," *Materials Research Bulletin*, vol. 113, pp. 182–189, 2019.

[23] S. Sonal and B. K. Mishra, "A comprehensive review on the synthesis and performance of different zirconium-based adsorbents for the removal of various water contaminants," *Chemical Engineering Journal*, vol. 424, p. 130509, 2021.

[24] C. Zhang, Y. Li, F. Wang et al., "Performance of magnetic zirconium-iron oxide nanoparticle in the removal of phosphate from aqueous solution," *Applied Surface Science*, vol. 396, pp. 1783–1792, 2017.

[25] A. Othmani, A. Kesraoui, and M. Seffen, "Removal of phenol from aqueous solution by coupling alternating current with biosorption," *Environmental Science and Pollution Research*, vol. 28, pp. 46488–46503, 2021.

[26] Y. Zheng, J. Liu, B. Cheng, W. You, W. Ho, and H. Tang, "Hierarchical porous Al_2O_3@ZnO core-shell microfibres with excellent adsorption affinity for Congo red molecule," *Applied Surface Science*, vol. 473, pp. 251–260, 2019.

[27] Z. Ma, C. Zhou, D. Wang et al., "Co-precipitated Fe-Zr catalysts for the Fischer-Tropsch synthesis of lower olefins (C_2O ~ C_4O): synergistic effects of Fe and Zr," *Journal of Catalysis*, vol. 378, pp. 209–219, 2019.

[28] G. Di, Z. Zhu, H. Zhang et al., "Simultaneous removal of several pharmaceuticals and arsenic on Zn-Fe mixed metal oxides: combination of photocatalysis and adsorption," *Chemical Engineering Journal*, vol. 328, pp. 141–151, 2017.

[29] H. Mo, J. Qiu, C. Yang, L. Zang, and E. Sakai, "Preparation and characterization of magnetic polyporous biochar for cellulase immobilization by physical adsorption," *Cellulose*, vol. 27, pp. 4963–4973, 2020.

[30] X. Liu, W. Zhang, L. Mao, Y. Yin, and L. Hu, "Synthesis of FeOCl-MoS_2 with excellent adsorption performance for methyl orange," *Journal of Materials Science*, vol. 56, pp. 6704–6718, 2021.

[31] X. Dou, Y. Zhang, H. Wang, T. Wang, and Y. Wang, "Performance of granular zirconium–iron oxide in the removal of fluoride from drinking water," *Water Research*, vol. 45, no. 12, pp. 3571–3578, 2011.

[32] Z. U. Ahmad, L. Yao, J. Wang et al., "Neodymium embedded ordered mesoporous carbon (OMC) for enhanced adsorption of sunset yellow: characterizations, adsorption study and adsorption mechanism," *Chemical Engineering Journal*, vol. 359, pp. 814–826, 2019.

[33] Y. Su, H. Cui, Q. Li, S. Gao, and J. K. Shang, "Strong adsorption of phosphate by amorphous zirconium oxide nanoparticles," *Water Research*, vol. 47, pp. 5018–5026, 2013.

[34] B. Moraga, L. Toledo, L. Jelinek, J. Yanez, B. L. Rivas, and B. F. Urbano, "Copolymer-hydrous zirconium oxide hybrid microspheres for arsenic sorption," *Water Research*, vol. 166, p. 115044, 2019.

[35] J. Wang and X. Guo, "Adsorption kinetic models: physical meanings, applications, and solving methods," *Journal of Hazardous Materials*, vol. 390, p. 122156, 2020.

[36] W. Zhang, W. Liu, G. Li et al., "Simultaneous adsorption and oxidation of para arsanilic acid by a highly efficient nanostructured Fe-Ti-Mn composite oxide," *Chemical Engineering Journal*, vol. 407, p. 127142, 2021.

[37] G. D. Değermenci, N. Değermenci, V. Ayvaoğlu, E. Durmaz, D. Çakır, and E. Akan, "Adsorption of reactive dyes on lignocellulosic waste; characterization, equilibrium, kinetic and thermodynamic studies," *Journal of Cleaner Production*, vol. 225, pp. 1220–1229, 2019.

[38] E. I. Ugwu, A. Othmani, and C. C. Nnaji, "A review on zeolites as cost-effective adsorbents for removal of heavy metals from aqueous environment," *International journal of Environmental Science and Technology*, 2021.

[39] H. Qian, Y.-L. Lin, B. Xu, L.-P. Wang, Z.-C. Gao, and N.-Y. Gao, "Adsorption of haloforms onto GACs: effects of adsorbent properties and adsorption mechanisms," *Chemical Engineering Journal*, vol. 349, pp. 849–859, 2018.

[40] N. Ayawei, A. N. Ebelegi, and D. Wankasi, "Modelling and interpretation of adsorption isotherms," *Journal of Chemistry*, vol. 2017, Article ID 3039817, 11 pages, 2017.

[41] H. Wang, Z. Li, S. Yahyaoui et al., "Effective adsorption of dyes on an activated carbon prepared from carboxymethyl cellulose: experiments, characterization and advanced modelling," *Chemical Engineering Journal*, vol. 417, p. 128116, 2021.

[42] X. Yao, L. Ji, J. Guo et al., "An abundant porous biochar material derived from wakame (Undaria pinnatifida) with high adsorption performance for three organic dyes," *Bioresource Technology*, vol. 318, p. 124082, 2020.

[43] J. Fan, Z. Zhao, W. Liu, Y. Xue, and S. Yin, "Solvothermal synthesis of different phase N-TiO$_2$ and their kinetics, isotherm and thermodynamic studies on the adsorption of methyl orange," *Journal of Colloid and Interface Science*, vol. 470, pp. 229–236, 2016.

[44] H. Molavi, A. Hakimian, A. Shojaei, and M. Raeiszadeh, "Selective dye adsorption by highly water stable metal-organic framework: long term stability analysis in aqueous media," *Applied Surface Science*, vol. 445, pp. 424–436, 2018.

[45] F. Guo, X. Jiang, X. Li, X. Jia, S. Liang, and L. Qian, "Synthesis of MgO/Fe$_3$O$_4$ nanoparticles embedded activated carbon from biomass for high-efficient adsorption of malachite green," *Materials Chemistry and Physics*, vol. 240, p. 122240, 2020.

[46] A. Malviya, D. K. Jaspal, and S. Khamparia, "Kinetics studies on the adsorption of methyl orange and metanil yellow onto bottom ash: a comparative account," *Water Science and Technology*, vol. 80, pp. 1844–1850, 2019.

[47] Y. Liu, L. Song, L. du et al., "Preparation of polyaniline/emulsion microsphere composite for efficient adsorption of organic dyes," *Polymers*, vol. 12, no. 1, 2020.

[48] L. Zhuannian, "Adsorption behavior of methyl orange onto modified ultrafine coal powder," *Chinese Journal of Chemical Engineering*, vol. 17, no. 6, pp. 942–948, 2009.

[49] B. Tanhaei, A. Ayati, E. Iakovleva, and M. Sillanpää, "Efficient carbon interlayed magnetic chitosan adsorbent for anionic dye removal: synthesis, characterization and adsorption study," *International Journal of Biological Macromolecules*, vol. 164, pp. 3621–3631, 2020.

[50] M. K. Uddin and U. Baig, "Synthesis of Co$_3$O$_4$ nanoparticles and their performance towards methyl orange dye removal: characterisation, adsorption and response surface methodology," *Journal of Cleaner Production*, vol. 211, pp. 1141–1153, 2019.